(Received 14 October 2024, Accepted 2 December 2024, Scheduled 21 December 2024)

Fracture Detection in Bone Tissue Models Using H-Slot Shaped Transceiver Resonators

Wongani Moyo[1, *], Ahmed Allam[1], Asano Tanemasa[2], and Adel B. Abdel-Rahman[1, 3]

[1] *Department of Electronics and Communications Engineering, EJUST, New Borg El-Arab City, Alexandria 21934, Egypt*
[2] *Graduate School of Information Science and Electrical Engineering Kyushu University Nishi Ku, Fukuoka 819-0395, Japan*
[3] *Electrical Engineering Department, Faculty of Engineering, South Valley University, Qena 83523, Egypt*

ABSTRACT: In this paper, a novel H-slot resonator of size 30 mm × 20 mm × 1.56 mm for fracture detection, backed with a perfect electric conductor (PEC), designed at 2.54 GHz is presented, and its performance is evaluated. Concurrently, an equivalent circuit model of the resonator is developed, and its performance coherently agrees with the CST model. The design is tested using a hybrid tissue phantom based on a second-order Debye dielectric tissue model. The detection of fractures of several thicknesses with a minimum width of 2 mm and a maximum of 10 mm was compared. Overall, the proposed design improves the detection of fractured regions in a bone with a 2 mm crack width as the smallest detectable crack size.

1. INTRODUCTION

In the era of Healthcare 4.0, also known as digital health, the transformation of healthcare delivery through the integration of advanced technologies makes sensors essential. Healthcare 4.0 builds on the concept of Industry 4.0, which focuses on using automation and data exchange in manufacturing [1]. In the pursuit of developing efficient and reliable medical devices for managing osteoporosis [2–4], bone fracture detection, and early arthritis detection, research has explored various technological avenues to optimize treatment outcomes for Healthcare 4.0 [5]. One notable area of exploration involves the utilization of microwave diagnosis techniques, which have shown promise in wireless power transfer (WPT) at relatively short distances, as reported by [6, 7]. The use of microwave antenna based monitoring has been studied by [7] in food monitoring; however, the use of a horn antenna as a transmitter and a rectangular waveguide as receiver results in sensor structures with large volume and irregular designs. This is in contrast to the design goal that posits that the use of planar structures with small design and volume guarantees miniaturization. Among the different electromagnetic structures investigated for this purpose, coupled resonators have emerged as a promising choice. As noted by [8], coupled resonators, characterized by their enhanced energy transfer through electromagnetic coupling, offer several advantages over traditional patch antennas in the context of bone fracture detection. While patch antennas have been widely employed in wireless communication systems, their suitability for medical applications, particularly the investigation of bone fractures, is limited by several factors. A notable factor is wavelength mismatch. In the 1–6 GHz frequency range, traditional antennas have wavelengths much larger than the size of small bones, limiting the imaging resolution, according to [9–11]. This mismatch in size limits the ability to interact effectively with the bone's material properties and detect subtle changes caused by fractures, resulting in low sensitivity [12].

In contrast, coupled resonators are adept at generating strong and uniform electromagnetic fields over a broader frequency range [12]. This attribute is crucial for ensuring effective stimulation of bone tissue fractures, as optimal detection outcomes often depend on the ability to deliver precise and controlled electromagnetic stimuli to the fracture site [10]. The application of dielectric resonators in sensing has been reported in work by [13] for the assessment of cracks in metal. However, metal is not a dispersive material, and hence its performance cannot be used as a basis for comparison in tissue models. Furthermore, the design is a large and complex structure that enables high power transmission but is only suitable for regular and dimensionally correct structures. Therefore, its use in irregular structures, including human limbs, is undesirable due to its high Specific Absorption Rate (SAR). Coupled resonators offer enhanced efficiency in energy transfer compared to patch antennas, minimizing power consumption and maximizing therapeutic efficacy [14]. This efficiency is particularly advantageous in implantable medical devices where battery life and patient comfort are paramount considerations.

Overall, the growing body of research reported by [15, 16] supporting the efficacy of coupled resonators in wireless power transfer underscores their potential to revolutionize the field of orthopedic medicine and imaging. By harnessing the principles of electromagnetic resonance, coupled resonator-based technologies hold promise for delivering targeted, efficient imaging and diagnosis [17] that promote accelerated bone regeneration and improved patient outcomes. Slots produce multiple benefits in the design metrics of an antenna or resonator according to various studies by [18–21] who used E-shaped slots to produce multiband resonances [18], L-shaped slots to achieve dual-band performance, U-shaped slots to improve bandwidth

* Corresponding author: Wongani Moyo (wongani.moyo@ejust.edu.eg).

[19] or even triangular slots to produce multiple resonances or reduce capacitive effects of the coxial probe, thereby improving matching [21]. The selection of the H-slot design herein provides excellent coupling, as evidenced through studies by [8]. The realized work makes contributions to the existing body of microwave sensing literature in several ways.

Achievements:

- The primary achievement is the miniaturization of the size of the overall structure. This addresses the challenge in microwave sensing arising from the trade-off between design size and optimal power transfer. The compact size of the resonator (30 mm × 20 mm1.56 mm) makes it suitable for integration into portable medical devices, promoting ease of use.
- The proposed H-slot resonator design achieves high detection accuracy for fractured regions in bone tissue, demonstrating sensitivity to fractures as small as 2 mm in width.
- We develop and validate an equivalent circuit model for the resonator, showing coherent agreement with the Computer Simulation Technology (CST) model and confirming the reliability of the design.
- The introduction of Perfect Electric Conductor(PEC)backing significantly enhances the resonator's performance, improving the S_{21} parameter to approximately -3.5 dB at a 50 mm separation distance between the transmitting and receiving resonators.
- The resonator's performance in a hybrid tissue phantom based on a second-order Debye model demonstrates its potential for practical applications in biomedical imaging and fracture detection.

A study by [22] on hepatic tumour microwave ablation of 48 patients using 915 MHz and 2.45 GHz systems showed that the 2.45 GHz system demonstrated that the mean total energy applied per lesion (per cm/min) was higher. This study concluded that 2.45 GHz has better radiation efficiency than 915 MHz. Therefore, the selection of the 2.54 GHz range is due to its vicinity to the 2.45 GHz to attain optimal radiation efficiency. The level of power from the Vector Network Analyzer (VNA) used in our work is 0 dBm which is lower and sufficient for the detection. In this work, the enhancement of maximum transferred power between two resonators is investigated through the incorporation of a PEC at the back of the resonator. The design is tested in fracture detection using a tissue phantom. The subsequent sections of the work are organized as follows. Section 2 presents the design, performance, and simulation results of the proposed design, and Section 3 focuses on tissue modeling using second-order Debye models. Section 4 details the experimental results of the realized resonator and phantom prototypes. Lastly, Section 5 concludes the paper.

2. RESONATOR DESIGN

2.1. H-Shape Configuration

Figure 1 provides the topology of the proposed H-slot resonator design made on a double-clad copper Rogers 4003C substrate

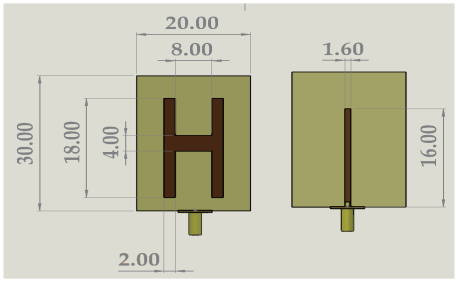

FIGURE 1. Dimensions of the resonator.

with a thickness of 0.813 mm ($\epsilon_r = 3.55$ and $\sigma = 0.0027$). An H-slot is etched onto the surface of the resonator and fed at the position shown in Fig. 2 with a 50 Ω SMA connector. The guided wavelength, λ_g, is crucial in determining both the slot length and the spacing between slots in a waveguide. Unlike the free-space wavelength (λ_0), λ_g is influenced by the relative permittivity (ϵ_r) of the dielectric material inside the waveguide [9, 14]. For this design, where $\epsilon_r = 3.55$ and the operating frequency is 2.54 GHz, the guided wavelength is calculated as:

$$\lambda_g = \frac{30}{f \cdot \sqrt{\epsilon_r}} = \frac{30}{2.54 \cdot \sqrt{3.55}} \approx 62.7\,\text{mm} \qquad (1)$$

To ensure efficient radiation, each slot length and spacing is approximately half of the guided wavelength, $\lambda_g/2$, yielding a slot length and spacing of $\lambda_g/2 = 31.35$ mm. With $\lambda_g/2$ for slot length and spacing, this design ensures optimal radiation efficiency at 2.54 GHz. The choice of $\epsilon_r = 3.55$ supports the desired frequency, making it suitable for applications requiring directional radiation patterns. This approach enabled optimal configuration specifically for the Industrial, Scientific, and Medical (ISM) band range. Finally, a parametric sweep was used as an efficient means to achieve the desired frequency response. A copper plate is placed approximately a quarter wavelength below the feedline to maximize the reduction of backward radiation.

2.2. Operating Principle and Design Optimization

A single H-slot resonator is designed as a band-pass filter connected via a single port. The H-slot resonator design is modeled in CST software and simulated to compare the performance analysis. It is worth noting that an H-slot resonator presented herein is a bandpass as conceived by [8] which can be modeled as a circuit whose parameters are given as in Fig. 8. The results show that the design resonates at 2.54 GHz and has an approximated -10 dB as the S_{21} forward radiated power. The simulated and measured results of the single resonator without a PEC are provided in Fig. 7 showing good coherence between the two cases. While the design operates well at relatively small distances, there is a challenge when the separation distance between the resonators is enlarged as the design has a drastic reduction in coupling and total transmitted power. As evident in the parametric analysis performed at the different distances, the power drops from approximately -10 dB at 10 mm separation distance to -28 dB 50 mm as portrayed in Fig. 4. This renders the H-slot resonator for power transfer at larger distances

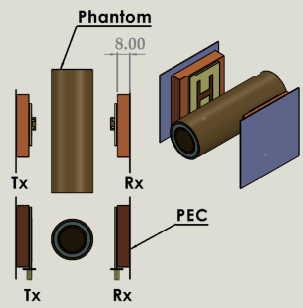

FIGURE 2. Proposed coupled resonator configuration with phantom included.

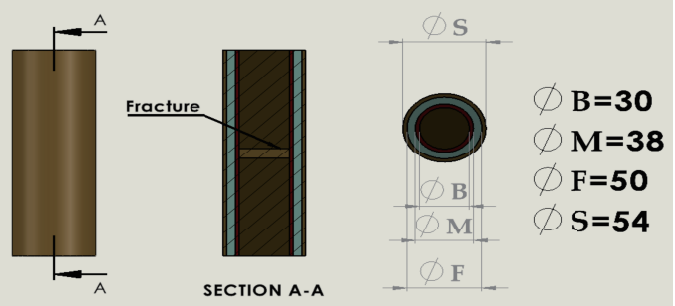

FIGURE 3. Phantom: ϕB (bone/blood), ϕM (muscle), ϕF (fat), ϕS (skin).

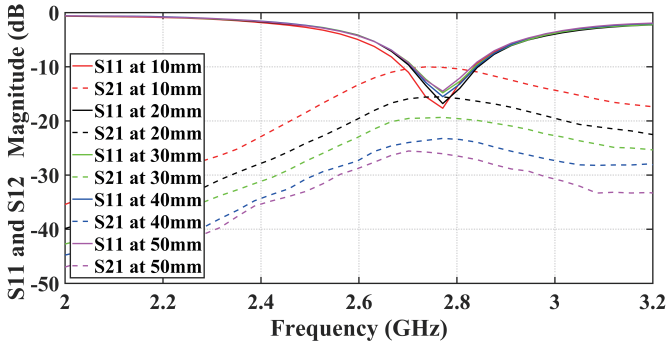

FIGURE 4. Resonator without PEC at different separation distances.

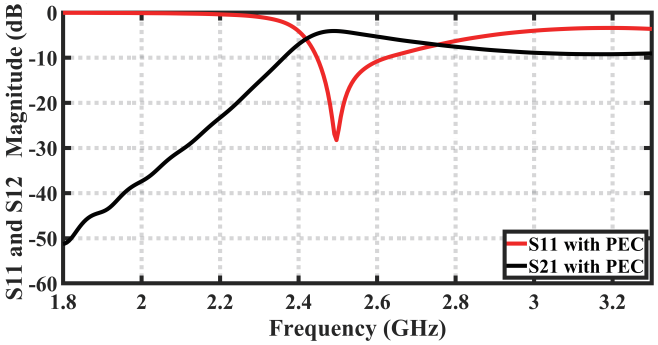

FIGURE 5. H-slotted back of resonator in CST with PEC.

obsolete in biomedical applications especially dispersive tissue exhibiting reflections and attenuation.

An H-slot designed without a PEC layer provides unimpeded wave propagation. Thus, the electromagnetic waves generated by the H-slot can freely propagate outward in both directions (forward and backward). This reduces the field concentration within the slot and weakens the resonance. Therefore, the work herein proposed introduces a PEC layer with dimensions of 60 mm by 60 mm, which allows forward-radiation and enhances coupling. An H-slot resonator utilizes a slot etched in a conducting plane to trap electromagnetic waves. This creates a region of localized, intense electric and magnetic fields. The PEC placed behind the H-slot acts as a reflector. It reflects the propagating electromagnetic waves toward the slot, essentially creating a cavity. The PEC ensures that the fields are reflected and remain concentrated within the slot region. A cornered reflector was used to improve the gain of an ultra-wideband antenna [23]. On-body antenna-based biological application systems require that the field penetrates the tissues, but no field is required on the other half-space [11]. In this regard, the backing of PEC simultaneously achieves higher gain and less back-radiation, proving itself as an effective antenna backing structure. The reflected waves from the PEC interfere with the incident waves, forming a standing wave pattern within the slot. This standing wave pattern is crucial for achieving resonance, where specific frequencies constructively interfere, maximizing the field intensity. Removing the PEC alters these electrical properties, potentially slightly shifting the resonant frequency away from the desired value.

While the already provided design exhibits resonance at 2.54 GHz, the introduction of a PEC layer alters the resonance frequency. In essence, the PEC backing acts as a critical boundary condition for an H-slot resonator. It confines the electromagnetic fields, establishes a resonant standing wave pattern, and maintains the electrical properties necessary for resonance at the designed frequency. Thus, the PEC sheet was positioned to allow for minimal frequency deviation. The new topology offers a resonance at 2.54 GHz and significantly improves the S_{21} to approximately -3.5 dB at a separation distance of 50 mm which is a key aspect being investigated. The improved design performance is presented in Fig. 5 and Fig. 6 which show a significant improvement in the S_{21} curve.

2.3. Equivalent Circuit Modelling

H-shaped resonators can be modeled using resistor, inductor, and capacitor (RLC) or LC circuits to validate conceived designs [8, 13, 24, 25]. The first step in realizing a band-pass filter is to develop a single pole band-stop filter that is connected by two ports. Such a circuit is simulated as presented in Case A of Fig. 8, and its results are used to extract f_C, the cutoff frequency, and f_0, the center frequency of the band-stop filter. The obtained values of f_C and f_0 were 1.6 GHz and 4.8 GHz, respectively. The determinant parameters of the resonance frequencies are circuit parameters C_P and L_P that are defined by Eqs. (2) and (3), respectively. The band-stop filter is converted into a band-pass filter by making it a single resonator and adjusting the feedline W_F to realize a certain resonant frequency [26]. This evolution is shown in Case B of Fig. 8 where

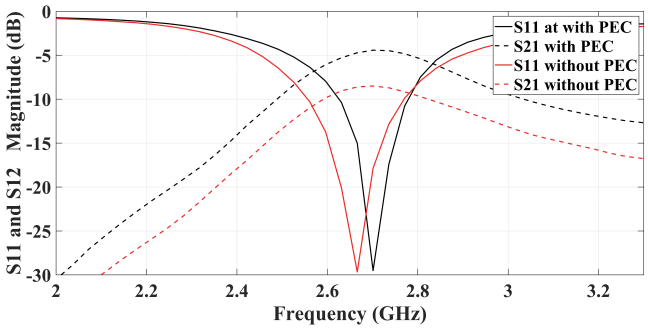

FIGURE 6. Comparing S-parameters with and without PEC.

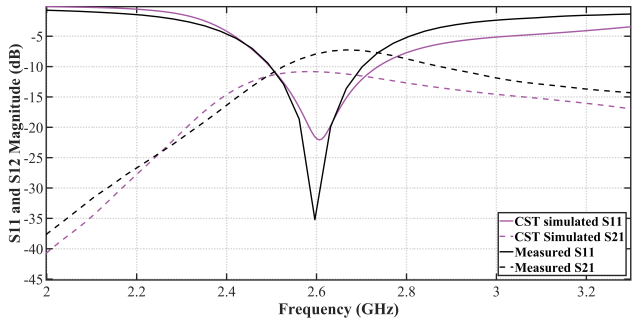

FIGURE 7. S-parameters of the proposed design.

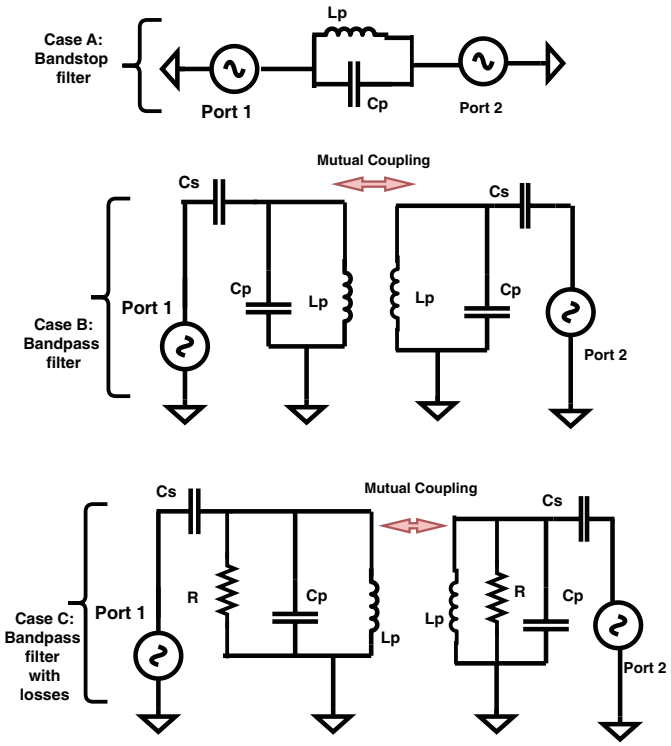

FIGURE 8. Equivalent circuit design process.

the resonator circuits are shown in coupled mode.

$$C_P = \frac{5f_C}{\pi(f_0^2 - f_C^2)} \tag{2}$$

$$L_P = \frac{250}{C_P[\pi f_0]^2} \tag{3}$$

where f_C is the lower cutoff frequency of the bandstop, and f_0 is the band-stop frequency. The introduction of the stub in the circuit results in modification of the circuit to give capacitor C_S in parallel to C_P and L_P if losses are neglected. To obtain C_S, Equation (4) is defined as:

$$C_S = \frac{1}{4\pi^2 f_s^2 \left[\frac{L_P}{1-(\frac{f_C}{f_0})^2}\right]} \tag{4}$$

where f_S is the resonance frequency of the coupled resonator. Additionally, the already stated values of f_C and f_0 with $f_S = 2.54\,\text{GHz}$ are used. The EM realized circuit and the S-parameters values are presented in Fig. 8. The realized circuit has been compared to the simulation realized resonator. As shown in Fig. 8, the circuit designed for the H-resonator with a PEC backing is assumed to have a symmetry plane about the X-axis, allowing for two similar circuit blocks that can be merged to produce the final circuitry. The circuit presented in Fig. 8 offers better performance. To verify the overall performance of the equivalent circuits versus the antenna models, a plot of the S-parameters is made. To introduce the losses that are incurred in the circuit, resistor R is introduced as shown in Case C of Fig. 8. The value of resistor R, is realized via an iterative process. Such an approach provides S_{21}, which is similar to the CST model result. The optimized circuit and the corresponding performance curves are presented in Fig. 9.

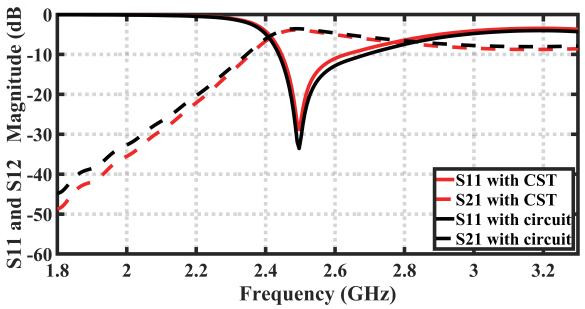

FIGURE 9. Optimized RLC circuit versus CST design performance.

3. MODELLING OF TISSUES USING SECOND-ORDER DEBYE MODEL

3.1. Mathematical Model for Tissues

Several established models exist, including Gabriel's model [27], Cole-Cole model [28], and Debye model [29], each offering varying levels of complexity and accuracy in the precise modeling of electromagnetic wave interactions with human tissue, which is paramount across numerous medical disciplines.

The Debye model, particularly its second-order iteration, presents a compromise between computational efficiency and accuracy for a wide range of tissue types [29]. This fundamental model describes the interaction of an electric field with a polar molecule, encompassing the relaxation process of the molecule's electric dipole moment. The first-order Debye

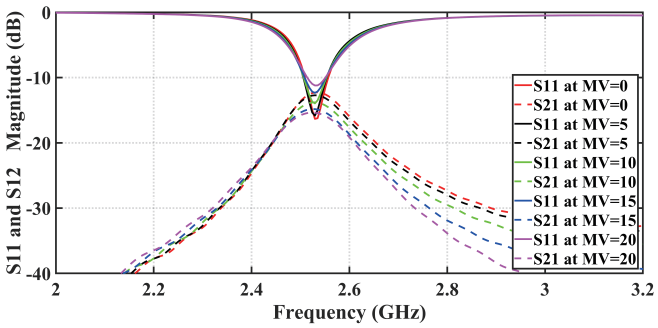

FIGURE 10. Simulated data S_{11} and S_{21} plot.

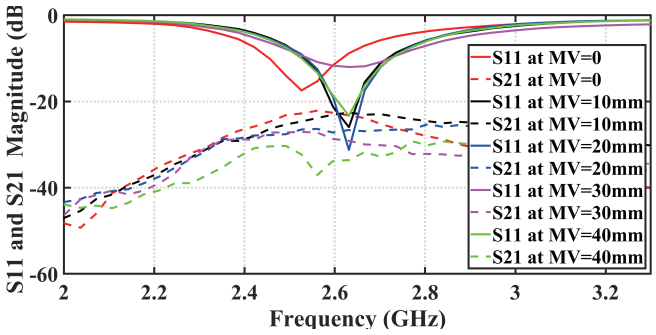

FIGURE 11. Measured data S_{11} and S_{21} plot.

model employs a single relaxation time, as expressed in the following equation:

$$\varepsilon(\omega) = \varepsilon_\infty + \frac{\varepsilon_s - \varepsilon_\infty}{1 + j\omega\tau} \tag{5}$$

where $\varepsilon(\omega)$ represents the complex permittivity of the tissue at a specific angular frequency Ω, ε_s the static permittivity, ε_∞ the infinite frequency permittivity, and τ the relaxation time. Recognizing the inherent heterogeneity of tissues, the second-order Debye model incorporates two relaxation times, leading to a more faithful representation [30]. The equation is approximated to:

$$\varepsilon(\omega) = \varepsilon_\infty + \frac{\varepsilon_s^{(1)} - \varepsilon_\infty}{1 + j\omega\tau_1} + \frac{\varepsilon_s^{(2)} - \varepsilon_\infty}{1 + j\omega\tau_2} \tag{6}$$

where $\varepsilon_s^{(1)}$ and $\varepsilon_s^{(2)}$ represent the static permittivity associated with the two relaxation processes while τ_1 and τ_2 are the corresponding relaxation times.

As [29] notes, additional relaxation time enables a superior fit to measure the dielectric properties of tissues over a broader frequency spectrum. While this enhanced accuracy comes with a slight increase in computational cost compared to the first-order model, the second-order Debye model often proves to be a highly effective approach due to its ability to capture the essential electrical behavior of tissues while maintaining computational efficiency. Conversely, models like Gabriel's model and Cole-Cole model [28] delve deeper into the complexity, incorporating additional dispersion mechanisms. However, the second-order Debye model frequently strikes an optimal balance, hence its adoption in our work. Following the work of [30], we adopted the second-order Debye model tissue parameters as calculated therein for the different layers of human tissue.

3.2. Modeling and Simulation of Fracture Detection

A phantom modeled using CST software based on the second-order is presented in Fig. 3 with values devised by [5]. To investigate the ability of the designed system in the presence of dispersive tissue material, the phantom is inserted with parameters defined in the system design shown in Fig. 2. Modeled as a discontinuity, the fractured region is a disc of varying thickness varying from 1 mm to 8 mm, and the coupled system is assumed to be a transceiver system where the phantom being studied is located in between coupled resonator, as displayed in Fig. 2.

The first task was to investigate the effect of the blood region on the S_{21} parameter curves. This is the equivalent of sensitivity analysis in the proposed model. Therefore, a comparison of the effect of the crack width defined as the parameter *Fw* in Fig. 15 was performed by increasing the thicknesses of the blood region in the fracture location. Fig. 15 shows that there was a noticeable difference of approximately 4 dB between the S_{21} curve at 1 mm thickness going up to 8 mm.

Secondly, the variation in the transferred power between the fractured region and normal region was investigated. With the location of the crack as a zero point, the phantom was moved in steps of $Mv = 5$ mm (with MV as the defined step sweeping parameter,) for a length range of -40 mm to 40 mm, and eventually, different regions of the phantom were evaluated for the changes in the S-parameters. It is evident from the plots that as the distance near the fracture point there was an increase in the S_{21} curve because a layer of blood caused variation in signal power. Fig. 10 portrays the discrepancy between the fractured and non-fractured regions of the bone especially in the S_{21} curve. At the centre of the fracture designated as $MV = 0$ mm, the S_{21} value is the highest unlike the last point $MV = 20$ mm. To further characterize the non-fractured and fractured regions, additional analysis was done by comparing the electric field distribution between the respective regions of the model. This analysis is presented in Fig. 12(a) and Fig. 12(b). Two cases are presented: firstly the electric field distribution in the non-fractured bone region in Fig. 12(a) and secondly the electric field distribution in a fractured region in Fig. 12(b). The focus is the overall field concentration on the receiver after the electric field propagates across the model. As represented in Fig. 12(a), the receiving resonator (denoted as Rx) in the non-fractured bone region shows lower electric field distribution. This is compared against Fig. 12(b) (fractured region), where the receiving resonator in the fractured region exhibited higher and more concentrated field distribution. This supports the S-parameter analysis where the cracked regions showed higher S_{21} values.

4. EXPERIMENTAL RESULTS

The designed resonator pairs and PEC sheets were fabricated and measured using a Keysight N5227A PNA Microwave Net-

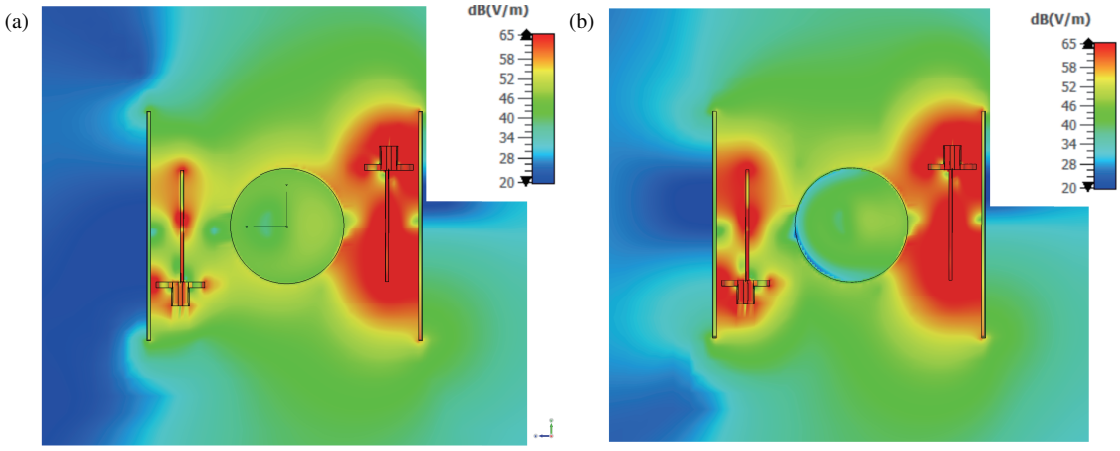

FIGURE 12. Electric field distribution in non-fractured and fractured regions. (a) Non-fractured region. (b) Fractured region. (a) Electric field distribution: Coupled resonators located in non-fractured region. (b) Electric field distribution: Coupled resonators located at fractured region.

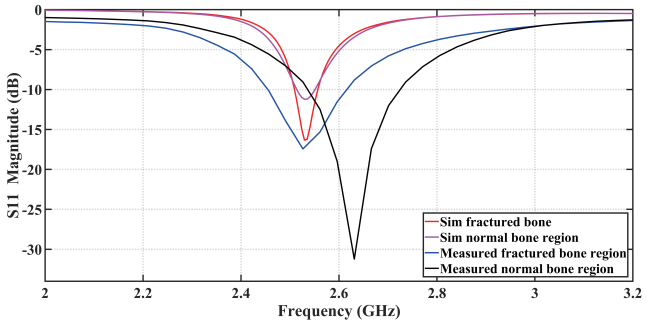

FIGURE 13. S_{11} values: Measured and simulated comparison.

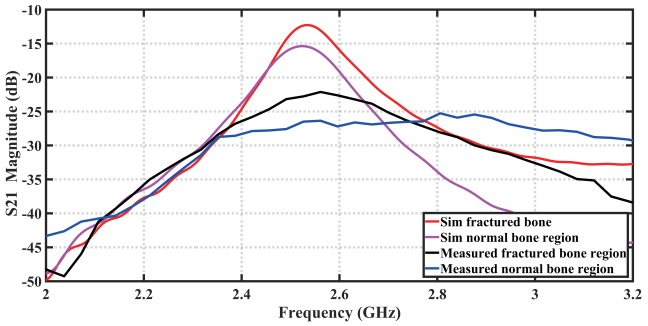

FIGURE 14. S_{21} values: Measured and simulated comparison.

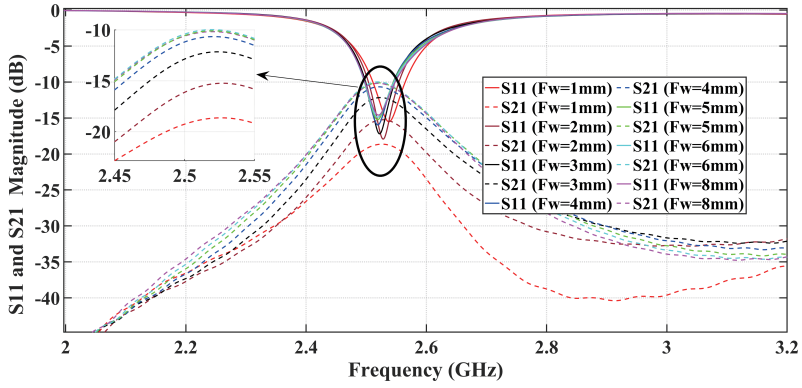

FIGURE 15. Crack width variation.

work Analyzer (10 MHz–67 GHz). As shown in Fig. 16, the resonator and PEC were separated by foam to create the separation distance. A representative comparison of the measured and simulated powers both in the circuit and the CST simulated power is provided in Fig. 7. These measured values are in agreement with the simulated ones.

To verify the simulation results, a bovine femur was used for measurements. The choice of material for measurement of experimental results is justified according to previous studies by [33, 35]. In their study, [35] used ex-vivo sheep femur bone for free space measurement experiments. The study used bone models for the feasibility of a deep neural network (DNN) approach for bone fracture diagnosis based on the noninvasive propagation of radio frequency waves. Therefore, bone is more comparable to the living tissue in human limbs. While actual bone tissues are irregular structures, we restricted the measurement to fairly regular regions. Thus, a bone model from an animal was used to show the practical performance of the tissue. The length of the femur was 300 mm, and a fracture of width 2 mm was made at a particular position within the length of the

TABLE 1. Comparison with existing work.

References	Dimensions	Frequency	Coupling Medium	Goal	Detection Mechanism	Crack configuration	Experimental	Comment
[5]	$0.36\lambda \times 0.36\lambda \times 0.037\lambda$	2.5 GHz	Free space and contact with specimen	1 mm-wide bone crack detection	Analysis of S-parameters and image reconstruction	Transverse and Longitudinal	Prototype made of semi-solid realized arm phantom	Miniaturized structure with PL based matching lens, Cascade of multiple layers difficult to fabricate
[31]	Vilvaldi antennas (Size unstated)	0.5–-4 GHz	Free space and contact with phantom	Reconstruction of bone profiles	S-parameters	Transverse	Tested on turkey tissues	No bone detection carried out, no coupling medium
[32]	$0.9\lambda \times 0.9\lambda \times 0.03\lambda$	8.3–11.1 GHz	Free space and no contact with phantom	1 mm-wide bone crack detection	S-parameters	Transverse	Tested on bovine tissues	Single crack analysis and bulky structure
[33]	Size unstated	2.45 GHz	Free space and contact with the measured body	1 mm wide detection	S-parameter and image reconstruction	Transverse	Porcine tissues added around dry human tibia	Low precision in the resonator design
[34]	$0.5\lambda \times 0.66\lambda \times 0.17\lambda$	3–7 GHz	Not Stated	Bone health evaluation and osteoporosis detection	Simulated S_{11} and S_{21}	Transverse	No experimental results	No wave propagation analysis, Single crack evaluated
Proposed work	$0.254\lambda \times 0.17\lambda \times 0.0132\lambda$	2.54 GHz	Free space and no contact with measured bone	2 mm-wide crack detection	Analysis of the changes in S_{21} magnitude	Transverse	Analysis on bone femur separated by gelatin-based blood layer	Resonator based design allows for power concentration, PEC sheet allows 5 dB gain in transmitted power

bone. The particular fractured region of 2 mm was replaced with a layer of modeled blood prepared with the ingredients as defined in [36, 37]. The specific ingredients include gelatin powder, salt (sodium chloride), cooking oil, and a detergent, all according to the prescribed weights and volume. The final measurement setup was provided in Fig. 17. The realized phantom was placed within the two coupled resonators (transmitter and receiver) to acquire experimental measurements with the VNA. The measurements were performed for two different scenarios: the coupled resonators alone with PEC and two complete systems (the coupled resonators alone with PEC), separated by the biological phantom. Firstly, the measurement was carried out

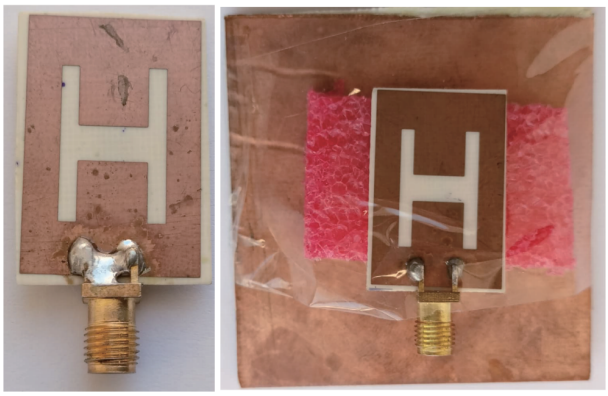

FIGURE 16. Left: Resonator PEC; Right: Resonator with PEC separated by foam.

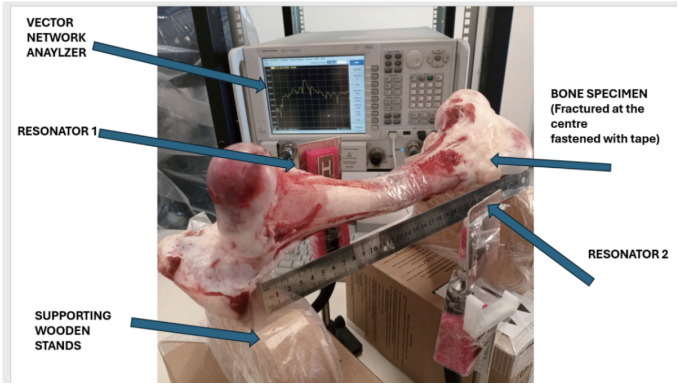

FIGURE 17. Measurement setup of the bone using vector network analyzer.

with the resonator located at the fracture position and gradually moved away from the fracture point while maintaining a step distance of 5 mm. The measured results suggested that at the fracture position, there was a high value of the transferred power as compared to the corresponding regions. As can be observed in Fig. 11 the 2.56 GHz range, at the location of the crack ($MV = 0$), there was an S_{21} value of -22 dB, and the next consecutive measured point ($MV = 10$ mm) away from the fractured position showed a lower S_{21} of -24 dB. In that similar order, we noticed that at 40 mm away (the furthest measured point) from the fracture point the S_{21} drops to -35 dB. Additionally, a comparison between the simulated and measured data was done and is presented in Fig. 14 and Fig. 13. Fig. 14 shows that in both simulation and measurement results, the normal bone region had a lower S_{21} while the fractured bone region had a high S_{21} value. A similar approach of comparison was the basis for bone health analysis by [5, 32]. In general, the simulated and measured results concurrently showed a noticeable decrease between consecutive points measured away from the fractured position. The differences in the measured and simulated results were due to the material differences as the bone used in the experiments had no uniform shape. Secondly, RF cable potential movement during scanning might have introduced undesirable phase and amplitude fluctuations leading to the stated deviations.

5. CONCLUSION

In this paper, an H-shaped resonator backed by a layer of PEC was designed, and its corresponding equivalent circuit was also presented. The realized design achieved an increase in the S_{21} over a traditional patch, thus allowing for better microwave imaging capabilities. By adopting a phantom model of bone tissue, simulated and measured results showed that the designed coupled resonator system can transfer significant power and detect a minute change in the crack thickness. Table 1 outlines existing works that have been performed. It is worth noting that the aforementioned design offers a significantly lower complexity in addressing the problem at hand whilst simultaneously transferring an improved amount of the S_{21} power through the realized phantom.

ACKNOWLEDGEMENT

This work was funded by the TICAD-7 scholarship in conjunction with JICA and the Egypt-Japan University and Technology collaboration.

REFERENCES

[1] Wehde, M., "Healthcare 4.0," *IEEE Engineering Management Review*, Vol. 47, No. 3, 24–28, 2019.

[2] Amin, B., A. Shahzad, L. Crocco, M. Wang, M. O'Halloran, A. González-Suárez, and M. A. Elahi, "A feasibility study on microwave imaging of bone for osteoporosis monitoring," *Medical & Biological Engineering & Computing*, Vol. 59, 925–936, 2021.

[3] Ghosh, D. and P. K. Sahu, "Osteoporosis detection with microwave signals: An investigation into natural resonance frequencies," *Sensors and Actuators A: Physical*, Vol. 365, 114867, 2024.

[4] Khalesi, B., B. Sohani, N. Ghavami, M. Ghavami, S. Dudley, and G. Tiberi, "Free-space operating microwave imaging device for bone lesion detection: A phantom investigation," *IEEE Antennas and Wireless Propagation Letters*, Vol. 19, No. 12, 2393–2397, 2020.

[5] Nouri Moqadam, A. and R. Kazemi, "Design of a novel dual-polarized microwave sensor for human bone fracture detection using reactive impedance surfaces," *Scientific Reports*, Vol. 13, No. 1, 10776, 2023.

[6] Makarov, S. N., G. M. Noetscher, S. Arum, R. Rabiner, and A. Nazarian, "Concept of a radiofrequency device for osteopenia/osteoporosis screening," *Scientific Reports*, Vol. 10, No. 1, 3540, 2020.

[7] Tai, T.-C., H.-W. Wu, C.-Y. Hung, and Y.-H. Wang, "Food security sensing system using a waveguide antenna microwave imaging through an example of an egg," *Sensors*, Vol. 20, No. 3, 699, 2020.

[8] Hekal, S. and A. B. Abdel-Rahman, "New compact design for short range wireless power transmission at 1 GHz using H-slot resonators," in *2015 9th European Conference on Antennas and Propagation (EuCAP)*, 1–5, Lisbon, Portugal, Apr. 2015.

[9] Pozar, D. M., *Microwave Engineering*, John Wiley & Sons, 2011.

[10] De Oliveira, A. M., A. M. d. O. Neto, M. B. Perotoni, N. Nurhayati, H. Baudrand, A. d. Carvalho, and J. F. Justo, "A fern antipodal vivaldi antenna for near-field microwave imaging medical

applications," *IEEE Transactions on Antennas and Propagation*, Vol. 69, No. 12, 8816–8829, 2021.

[11] Brizi, D., M. Conte, and A. Monorchio, "A performance-enhanced antenna for microwave biomedical applications by using metasurfaces," *IEEE Transactions on Antennas and Propagation*, Vol. 71, No. 4, 3314–3323, 2023.

[12] He, G., "Dual-band and dual-polarized antenna for wearable application," in *2018 11th UK-Europe-China Workshop on Millimeter Waves and Terahertz Technologies (UCMMT)*, Vol. 1, 1–3, Hangzhou, China, Sep. 2018.

[13] Wang, Q., K. Bi, Y. Hao, L. Guo, G. Dong, H. Wu, and M. Lei, "High-sensitivity dielectric resonator-based waveguide sensor for crack detection on metallic surfaces," *IEEE Sensors Journal*, Vol. 19, No. 14, 5470–5474, 2019.

[14] Balanis, C. A., *Antenna Theory: Analysis and Design*, John Wiley & Sons, 2015.

[15] Sample, A. P., D. T. Meyer, and J. R. Smith, "Analysis, experimental results, and range adaptation of magnetically coupled resonators for wireless power transfer," *IEEE Transactions on Industrial Electronics*, Vol. 58, No. 2, 544–554, 2010.

[16] Joannopoulos, J. D., A. Karalis, and M. Soljacic, "Wireless energy transfer using coupled resonators," US Patent US20100117455A1, 2010.

[17] Sharquie, K. E., S. A. Al-Mashhadani, A. A. Noaimi, and W. B. Al-Zoubaidi, "Microwave thermotherapy: New treatment for cutaneous leishmaniasis," *Our Dermatology Online*, Vol. 6, No. 2, 125–129, 2015.

[18] Kucuk, E., B. Bayram, S. T. Imeci, and T. Durak, "E-shaped patch antenna at 4.87 GHz," in *2018 International Applied Computational Electromagnetics Society Symposium (ACES)*, 1–2, Denver, CO, USA, Mar. 2018.

[19] Deshmukh, A. A., M. Gala, and S. R. Agrawal, "U-slot cut shorted square microstrip antenna," in *2016 IEEE International Conference on Advances in Electronics, Communication and Computer Technology (ICAECCT)*, 221–225, Pune, India, Dec. 2016.

[20] Yadav, D., "L-slotted rectangular microstrip patch antenna," in *2011 International Conference on Communication Systems and Network Technologies*, 220–223, Katra, India, Jun. 2011.

[21] Burcakbas, A., S. Soylu, B. Bektas, and S. T. Imeci, "Square shape patch antenna with triangular slot," in *2017 International Applied Computational Electromagnetics Society Symposium — Italy (ACES)*, 1–2, Firenze, Italy, Mar. 2017.

[22] Simo, K. A., V. B. Tsirline, D. Sindram, M. T. McMillan, K. J. Thompson, R. Z. Swan, I. H. McKillop, J. B. Martinie, and D. A. Iannitti, "Microwave ablation using 915-MHz and 2.45-GHz systems: What are the differences?" *HPB*, Vol. 15, No. 12, 991–996, 2013.

[23] Trimukhe, M. A. and B. G. Hogade, "Gain enhancement of compact UWB antenna using planar reflector," in *2019 International Conference on Communication and Electronics Systems (ICCES)*, 1444–1446, Coimbatore, India, Jul. 2019.

[24] Haack, M. P., R. P. Jenkins, W. Mai, G. Mackertich-Sengerdy, S. D. Campbell, M. F. Pantoja, and D. H. Werner, "Physically realizable antenna equivalent circuit generation," *IEEE Access*, Vol. 12, 33 652–33 658, 2024.

[25] Hong, J.-S. G. and M. J. Lancaster, *Microstrip Filters for RF/Microwave Applications*, John Wiley & Sons, 2004.

[26] Abdel-Rahman, A. B. and A. S. Omar, "Miniaturized bandpass filters using capacitor loaded folded slot coupled resonators," in *IEEE Middle East Conference on Antennas and Propagation (MECAP 2010)*, 1–4, Cairo, Egypt, Oct. 2010.

[27] Gabriel, S., R. W. Lau, and C. Gabriel, "The dielectric properties of biological tissues: III. Parametric models for the dielectric spectrum of tissues," *Physics in Medicine & Biology*, Vol. 41, No. 11, 2271, 1996.

[28] Cole, K. S. and R. H. Cole, "Dispersion and absorption in dielectrics I. Alternating current characteristics," *The Journal of Chemical Physics*, Vol. 9, No. 4, 341–351, 1941.

[29] Ireland, D. and A. Abbosh, "Optimised second-order Debye parameters for head tissues at microwave frequencies," in *Proceedings of the 2012 IEEE International Symposium on Antennas and Propagation*, 1–2, Chicago, IL, USA, Jul. 2012.

[30] Eleiwa, M. A. and A. Z. Elsherbeni, "Debye constants for biological tissues from 30 Hz to 20 GHz," *Applied Computational Electromagnetics Society Journal*, Vol. 16, No. 3, 202–213, 2001.

[31] Ruvio, G., A. Cuccaro, R. Solimene, A. Brancaccio, B. Basile, and M. J. Ammann, "Microwave bone imaging: A preliminary scanning system for proof-of-concept," *Healthcare Technology Letters*, Vol. 3, No. 3, 218–221, 2016.

[32] Santos, K. C., C. A. Fernandes, and J. R. Costa, "Feasibility of bone fracture detection using microwave imaging," *IEEE Open Journal of Antennas and Propagation*, Vol. 3, 836–847, 2022.

[33] Ramalingam, V. S., M. Kanagasabai, and E. F. Sundarsingh, "A compact microwave device for fracture diagnosis of the human Tibia," *IEEE Transactions on Components, Packaging and Manufacturing Technology*, Vol. 9, No. 4, 661–668, 2019.

[34] Kerketta, S. R. and D. Ghosh, "Microwave sensing for human bone health evaluation," *AEU — International Journal of Electronics and Communications*, Vol. 127, 153469, 2020.

[35] Beyraghi, S., F. Ghorbani, J. Shabanpour, M. E. Lajevardi, V. Nayyeri, P.-Y. Chen, and O. M. Ramahi, "Microwave bone fracture diagnosis using deep neural network," *Scientific Reports*, Vol. 13, No. 1, 16957, 2023.

[36] Yilmaz, T., R. Foster, and Y. Hao, "Broadband tissue mimicking phantoms and a patch resonator for evaluating noninvasive monitoring of blood glucose levels," *IEEE Transactions on Antennas and Propagation*, Vol. 62, No. 6, 3064–3075, 2014.

[37] Redzwan, S., N. B. Asan, J. Velander, D. Lee, M. D. Perez, M. Raaben, T. J. Blokhuis, and R. Augustine, "Frequency domain analysis of hip fracture using microwave split ring resonator sensor on phantom model," in *2016 IEEE Asia-Pacific Conference on Applied Electromagnetics (APACE)*, 244–247, Langkawi, Malaysia, Dec. 2016.